

Dense Outflowing Molecular Gas in Massive Star-forming Regions

YANI XU,¹ JUNZHI WANG,^{1,*} SHU LIU,² JUAN LI,^{3,4} YUQIANG LI,^{3,5} RUI LUO,¹ CHAO OU,¹ SIQI ZHENG,^{3,4,5} AND YIJIA LIU⁶

¹*Guangxi Key Laboratory for Relativistic Astrophysics, School of Physical Science and Technology, Guangxi University, Nanning 530004, China*

²*National Astronomical Observatories, Chinese Academy of Sciences, Beijing 100101, People's Republic of China*

³*Shanghai Astronomical Observatory, Chinese Academy of Sciences, No. 80 Nandan Road, Shanghai, 200030, China*

⁴*Key Laboratory of Radio Astronomy, Chinese Academy of Sciences, Nanjing 210033, China*

⁵*School of Astronomy and Space Sciences, University of Chinese Academy of Sciences, No. 19A Yuquan Road, Beijing 100049, People's Republic of China*

⁶*Department of Physics, Anhui Normal University, Wuhu, Anhui 241002, People's Republic of China*

(Dated: June 14, 2024)

ABSTRACT

Dense outflowing gas, traced by transitions of molecules with large dipole moment, is important for understanding mass loss and feedback of massive star formation. HCN 3-2 and HCO⁺ 3-2 are good tracers of dense outflowing molecular gas, which are closely related to active star formation. In this study, we present on-the-fly (OTF) mapping observations of HCN 3-2 and HCO⁺ 3-2 toward a sample of 33 massive star-forming regions using the 10-m Submillimeter Telescope (SMT). With the spatial distribution of line wings of HCO⁺ 3-2 and HCN 3-2, outflows are detected in 25 sources, resulting in a detection rate of 76%. The optically thin H¹³CN and H¹³CO⁺ 3-2 lines are used to identify line wings as outflows and estimate core mass. The mass M_{out} , momentum P_{out} , kinetic energy E_K , force F_{out} and mass loss rate \dot{M}_{out} of outflow and core mass, are obtained for each source. A sublinear tight correlation is found between the mass of dense molecular outflow and core mass, with an index of ~ 0.8 and a correlation coefficient of 0.88.

Keywords: Star forming regions, molecular outflow

1. INTRODUCTION

Molecular outflows were first detected within the core of the Orion molecular cloud (Zuckerman et al. 1976; Kwan & Scoville 1976) and well studied in past decades (Shepherd & Churchwell 1996; Wu et al. 2004; Zhang et al. 2005). Numerous studies have shown the significant relevance of outflows to the evolution and feedback of star formation (Shu et al. 1987; Zhang et al. 2005; Bally 2016). Outflows form during the major accretion phase of protostellar evolution, serving as one of the earliest observable signatures of star formation (Bontemps & Andre 1997; Li et al. 2019; Liu et al. 2020). As stars originate from the gravitational collapse of molecular clouds, accretion disks form around the protostars. Molecular outflows play a crucial role in removing excess angular momentum from the accreting material, thus facilitating accretion and increasing the mass of protostellar cores (Shu et al. 1987, 2000; Königl & Pudritz 2000; Motte et al. 2010).

The emission lines of CO and SiO are tracers for detecting molecular outflows (Zhang et al. 2001, 2005; Guerra-Varas et al. 2023). Low- J CO lines are widely used to trace total molecular outflows in star-forming regions (Zuckerman et al. 1976; Kwan & Scoville 1976; Wu et al. 2004). SiO serves as a well-known tracer for molecular outflows, specifically indicating the presence of shocked gas resulting from outflow collisions with the surrounding environment (Martin-Pintado et al. 1992; Gusdorf et al. 2008; De Simone et al. 2022). However, the abundance of

* E-mail: junzhiwang@gxu.edu.cn

SiO emission is enhanced due to grain sputtering (Blake et al. 1995; Rodriguez et al. 2021), leading to significant uncertainties in obtaining outflow parameters with SiO lines.

Dense outflowing molecular gas, situated closer to the central source than outflows traced by low- J CO (Yang et al. 1991; Arce & Sargent 2006; Zinchenko et al. 2015), is more reflective of the evolution and feedback of active massive star formation, making it a powerful tool for studying the massive star-formation process (Lada et al. 2010; Heiderman et al. 2010). Transitions of molecules with large dipole moments, such as lines of HCN, HCO⁺, HNC, and CS, etc, require high densities ($n > 10^4 \text{ cm}^{-3}$) for efficient excitation. They are almost unaffected by contamination from environmental gas emissions, making them well suited for tracing dense outflowing molecular gas.

Molecular outflows had been revealed with dense gas tracers and CO lines in past years. The mapping of the outflows toward the dark cloud L1287, traced by CO 1-0 and HCO⁺ 1-0, implies that the outflows are embedded in high-density gas and driven by a cold-type infrared source (Yang et al. 1991). CO 1-0 and HCO⁺ 1-0 outflows in low-mass protostars were imaged using OVRO millimeter array of six 10.4 m telescopes (Arce & Sargent 2006), indicating that dense gas from the outer regions of the circumstellar envelope, entrained by high-velocity flow, erodes the envelope and widens the outflow cavities. Zinchenko et al. (2015) found a more extended CO 3-2 outflow than that of high-density tracers in the massive star-forming region S255IR, indicating it is supposed to be driven by the jet bow shock mechanism. The mechanical luminosities, mass, mass-loss rates, and forces of outflows (¹²CO, ¹³CO, HCO⁺ 1-0, CS, SiO 2-1) toward nine nearby high-mass star-forming regions were studied with the 14 m millimeter telescope of the Purple Mountain Observatory (Liu et al. 2021). The morphology, kinematics, and energetics of the DR21 Main outflow traced by HCN, HCO⁺ 1-0 were studied with IRAM 30 m and NOEMA telescopes (Skretas et al. 2023), revealing it resemble a typical bipolar outflow. However, there still lacks sufficient studies on dense outflowing molecular gas in massive star-forming regions, particularly with large sample in the literature (Liu et al. 2021; Skretas et al. 2023), which could provide different informations compared to those obtained from CO observations. Furthermore, acquiring such information is crucial for enhancing our understanding of massive star-formation processes.

In this paper, we present HCO⁺, HCN, H¹³CO⁺ and H¹³CN 3-2 on-the-fly (OTF) observations toward a sample of 33 massive star forming regions with strong (>0.5K) H¹³CN 2-1 emissions in the Milky Way from Reid et al. (2014). The parallax measurements of this sample (Reid et al. 2014) were obtained using Very Long Baseline Interferometry techniques, providing accurate distances, which are crucial for reducing uncertainties in calculating parameters such as mass, mass-loss rate and force of molecular outflow in each source. The observations and data reductions are described in Sect. 2. Section 3 presents the calculation and results on outflows parameters. In Sect.4, we discuss the relationship between outflows and cores.

2. OBSERVATIONS AND DATA REDUCTION

The present study selects 33 massive star-forming regions from Reid et al. (2014) with parallax distances. The observations were carried out using the 10-m Submillimeter Telescope (SMT; Mt. Graham, Arizona) in the OTF mapping mode with 1.3 mm ALMA band 6 receiver. The OTF maps have sizes of $2' \times 2'$ regions for HCO⁺ 3-2 and HCN 3-2, $1.5' \times 1.5'$ for H¹³CO⁺ 3-2 and H¹³CN 3-2, respectively. The mapping center of each source is maser position from Reid et al. (2014) and presented in Table 1. The maps of HCO⁺ 3-2 at rest frequency of 267.557633 GHz and HCN 3-2 at rest frequency of 265.886431 GHz were obtained in the upper sideband (USB) simultaneously. The isotopic molecules, H¹³CO⁺ 3-2 with rest frequency of 260.255342 GHz and H¹³CN 3-2 with rest frequency of 259.011787 GHz were observed simultaneously also in the USB with the second tuning setup. The resulting maps have spatial resolution of $\sim 27.8''$ at 260 GHz and step size of $15''$ after re-gridding the OTF data of HCO⁺ 3-2 and HCN 3-2 for each source. The map of H¹³CO⁺ or H¹³CN 3-2 is gridded to match the center and each position of the spatial resolved HCO⁺ or HCN 3-2 data. The more detailed information can be found in Liu et al. (2023). The antenna temperature T_A^* is converted to main beam brightness temperature T_{mb} using the equation $T_{mb} = T_A^*/\eta_b$, where the main beam efficiency η_b is 0.77.

The data are reduced using the CLASS in GILDAS software package, following a specific process for each line of each source. At first, a refined average spectral line is obtained by averaging the spectral lines of all pixels in the mapping area to select line-free channels for baseline fitting. A first-order linear baseline fit is then applied to spectral line in each pixel. The spatially averaged H¹³CO⁺ and H¹³CN 3-2 lines are well fitted with single component Gaussian profile, which are used to define the velocity ranges of HCO⁺ and HCN 3-2 line wings. The ‘print area’ command is employed to obtain velocity integrated intensity for line wings in each pixel, as well as for the dense cores of H¹³CN and H¹³CO⁺ 3-2 lines.

3. RESULTS

3.1. Line profiles of HCN 3-2 and HCO⁺ 3-2

We identify outflows by inspecting the line wing emission in the HCO⁺ 3-2 & HCN 3-2 spectra. HCO⁺ 3-2 and HCN 3-2 are optically thin in line wing and optically thick in line core. The isotopic lines H¹³CO⁺ 3-2 and H¹³CN 3-2, which are normally optically thin, are used to identify the velocity ranges of line cores. The line wings of HCO⁺ 3-2 & HCN 3-2 are defined as the velocity ranges with HCO⁺ 3-2 & HCN 3-2 and without H¹³CO⁺ 3-2 & H¹³CN 3-2 emission. Such emission of HCO⁺ 3-2 and HCN 3-2 at lines wings are optically thin. The line wings of HCO⁺ 3-2 and HCN 3-2 obtained in this way for each source are considered as dense molecular outflows in subsequent analyses.

Fig. 1 presents the spatially averaged spectra of HCO⁺ 3-2 and HCN 3-2, as well as their isotopic lines, H¹³CO⁺ 3-2 and H¹³CN 3-2, for the 33 sources. In terms of spectral characteristics, the intensities between blue and red wings in most sources are similar, although certain sources exhibit significant differences, such as G005.88-00.39 and G043.16+00.01. Furthermore, the velocity ranges of the line wings for HCN 3-2 are generally wider than those of HCO⁺ 3-2. Among the 33 sources, a total of 25 were found to exhibit outflows, while the remaining eight showed no evidence of outflows. Within the subset of sources with outflows, 18 exhibited bipolar lobes traced by both HCO⁺ 3-2 and HCN 3-2, while 3 sources had a single lobe traced by both lines. Additionally, bipolar lobes were identified solely with HCO⁺ 3-2 in 2 sources, whereas in another 2 sources, the bipolar lobes were solely identified with HCN 3-2. The parameters for all sources are presented in Table 1.

3.2. Integrated intensity maps

Fig. 2 shows the velocity integrated maps of blue and/or red wings of HCO⁺ 3-2, overlaid on greyscale of H¹³CO⁺ 3-2. In Fig. 4, the velocity integrated maps of blue and/or red wings of HCN 3-2 are presented, with H¹³CN 3-2 as greyscale background.

Regarding HCO⁺ 3-2, clear bipolar morphology is found in 19 outflows, while 3 outflows exhibit only red lobes. In 7 sources, the locations between blue and red lobes can be well separated, with the largest observed separation of 54'' in G015.03-00.67, corresponding to a physical distance of 0.026 pc. In the remaining 12 sources, the lobes cannot be distinctly separated under the current spatial resolution. Furthermore, there are 11 sources where outflows are offset from the core centers. Similarly, for HCN 3-2, 19 outflows exhibit clear bipolar morphology, while 3 outflows exhibit only red lobes. The separation between blue and red lobes can be well resolved in 10 sources, including G015.03-00.67 where the largest observed separation of 54'' is noted. In the remaining 9 sources, the lobes cannot be clearly separated under the current spatial resolution. 9 sources show outflows offset from the core centers. The HCN 3-2 and HCO⁺ 3-2 outflows present different morphology in each source for 9 sources with blue and red lobes well separated, indicating that these outflows do have varying physical and/or chemical conditions at different regions. The observational parameters for all sources are listed in Table 2.

3.3. Parameters of outflows and cloud cores

3.3.1. The parameters with fixed abundance ratios

With the reasonable assumptions that HCO⁺ 3-2, HCN 3-2 at line wings and H¹³CO⁺ 3-2, H¹³CN 3-2 in cloud cores are optically thin under local thermodynamic equilibrium (LTE) conditions, the column densities of the molecules can be derived with

$$N_{tot} = \frac{8\pi k\nu^2}{hc^3 A_{ul}} \frac{Q(T_{ex})}{g_u} e^{E_u/kT_{ex}} \int T_{mb} dv \quad (\text{cm}^{-2}), \quad (1)$$

where k is the Boltzmann constant, h is the Planck constant, c is the speed of light, ν is the frequency of the molecular emission line, A_{ul} the Einstein emission coefficient, T_{ex} is the excitation temperature, and $Q(T_{ex})$ is the partition function, g_u is the upper-level degeneracy, E_u is the upper-level energy, and T_{mb} is the main beam temperature. The values of A_{ul} , $Q(T_{ex})$, g_u and E_u for the four molecular lines are from the Cologne Database for Molecular Spectroscopy ¹ (Müller et al. 2001, 2005). The values of $\int T_{mb} dv$ are the sum over the entire region condensed into a single beam. The assumption of $T_{ex} = 18.75$ K is used in the calculations of column density, as the impact of T_{ex} on results is not that significant. For example, when $T_{ex} = 37.5$ K, the calculated outflow mass is ~ 1.9 times of that obtained at 18.75 K, as also discussed for CO 3-2 with different T_{ex} (Skretas & Kristensen 2022).

¹ https://cdms.astro.uni-koeln.de/classic/predictions/catalog/partition_function.html

We first derive the outflow mass by using the assumed relative abundance $[\text{HCN}/\text{H}_2] = 5 \times 10^{-9}$ and $[\text{HCO}^+/\text{H}_2] = 2.3 \times 10^{-9}$ obtained in Orion (Blake et al. 1987), with

$$M = \frac{N_{tot} \times S_{beam} \times D^2 \times m_{\text{H}_2} \times H}{M_{\odot}}, \quad (2)$$

where N_{tot} is the column densities obtained before, S_{beam} denotes the area of the beam size in square radian, $m_{\text{H}_2} = 3.35 \times 10^{-24}$ g is the mass of a hydrogen molecule, H represent the relative abundance of HCN and HCO^+ with hydrogen, D is the distance of the source to the sun in cm, and M_{\odot} is the solar mass in g. It can also be used for calculating the mass of cloud cores with H^{13}CN 3-2 and H^{13}CO^+ 3-2 emission.

The mass loss rate is defined as

$$\dot{M}_{out} = M/t_{dyn}, \quad (3)$$

Subsequently, the outflow momentum is calculated as:

$$P_{out} = M_{out}v_{out}, \quad (4)$$

and the time-averaged kinetic energy of the outflow, is taken as

$$E_k = \frac{1}{2}M_{out}v_{out}^2 \quad (5)$$

also, the outflow force is obtained as

$$F_{out} = \dot{M}_{out}v_{out}, \quad (6)$$

where t_{dyn} represents the dynamical timescale of the outflow and is determined by the ratio between the linear size of the outflow along the flow axis (R_{out}) and its flow velocity (v_{out}). The method for estimating t_{dyn} involves calculating the ratio of the separation between the peak of the blue and red lobes to the mean outflow velocity (Cabrit et al. 1990; Zhang et al. 2005). Given the inherent difficulty in determining the orientation of the outflow, the inclination angle c_1 of 45° was used for the calculations. The impact of inclination angle was discussed in Cabrit et al. (1990). The resulting HCN outflow properties are presented in Table 2 and 3.

3.3.2. The parameters obtained without fixed HCO^+ abundance

The abundance $[\text{HCN}/\text{H}_2]$ is generally assumed to be similar in different Galactic molecular clouds. However, the abundance $[\text{HCO}^+/\text{H}_2]$ varies among different sources. Therefore, a crude method is used to obtain the abundance $[\text{HCO}^+/\text{H}_2]$ for each source with following assumptions, to calculate outflow mass traced by HCO^+ 3-2. First, the abundance ratio of ^{12}C to ^{13}C is equal to that of HCN & HCO^+ to H^{13}CN & H^{13}CO^+ . Second, the abundance ratio of ^{12}C to ^{13}C remains consistent between the outflow and cloud cores. Third, the cloud cores traced by H^{13}CN and H^{13}CO^+ are with identical mass. The abundance ratio of ^{12}C to ^{13}C in each source can be determined by Yan et al. (2023) based on the Galactocentric distance, with the following calculation formula:

$$^{12}\text{C}/^{13}\text{C} = (3.77 \pm 0.81)R_{GC} + (20.76 \pm 4.61). \quad (7)$$

The abundance $[\text{H}^{13}\text{CN}/\text{H}_2]$ in each source can be determined using the abundance $[\text{HCN}/\text{H}_2]$ and $^{12}\text{C}/^{13}\text{C}$ ratio. The mass of each cloud core can be calculated using equations (1) and (2) with H^{13}CN 3-2 line. Assuming that both H^{13}CN 3-2 and H^{13}CO^+ 3-2 trace the same dense core, the abundance $[\text{H}^{13}\text{CO}^+/\text{H}_2]$ can be calculated. Subsequently, the abundance $[\text{HCO}^+/\text{H}_2]$ in each source can be obtained with $^{12}\text{C}/^{13}\text{C}$ ratio. Note that inaccuracies in the ^{12}C to ^{13}C ratio in each source only affect the estimation of core mass, while the derived $[\text{HCO}^+/\text{H}_2]$ abundance and the outflow mass traced by HCO^+ 3-2 obtained in this way remain unaffected, as the ^{12}C to ^{13}C ratio cancels out during these calculations. Consequently, the outflow mass in each source, traced by HCO^+ 3-2, can be determined with the derived $[\text{HCO}^+/\text{H}_2]$ abundance. Furthermore, the mass-loss rate, momentum, kinetic energy, and force of outflow can be obtained. The calculated results with unfixed HCO^+ abundance are presented in Table 2 and Table 3.

The outflow masses in 25 of 33 massive star forming regions, as the summation of blue and red ones if both are detected, range from 0.28 M_{\odot} in G012.80-00.20 to 165.4 M_{\odot} in G043.16+00.01, with typical values in the tens of M_{\odot} range. The core masses vary widely from 3.95 M_{\odot} in G183.72-03.60 to 8730 M_{\odot} in G043.16+00.01. The dynamical timescales for dense outflowing molecular gas span from 2.6×10^3 to 6.6×10^4 yr. The mass-loss rates range from

2.1×10^{-5} to $5.2 \times 10^{-3} M_{\odot} \text{ yr}^{-1}$, with typical values in the range of 10^{-4} to $10^{-3} M_{\odot} \text{ yr}^{-1}$. The outflow momentum spans from a few to several thousand $M_{\odot} \text{ km s}^{-1}$, while the outflow kinetic energy ranges from a few to tens of thousands $M_{\odot} \text{ km}^2 \text{ s}^{-2}$. Additionally, outflow forces range from 8.1×10^{-5} to $3.44 \times 10^{-2} M_{\odot} \text{ km s}^{-1} \text{ yr}^{-1}$, with typical values between 10^{-3} and $10^{-2} M_{\odot} \text{ km s}^{-1} \text{ yr}^{-1}$.

Fig. 4 presents the plots of outflow mass from 25 sources. The abscissa indicates the outflow mass traced by HCN 3-2 and the ordinate indicates that traced by HCO^+ 3-2. In the left of Fig. 4, the outflow mass in each source traced by HCO^+ 3-2 was obtained with fixed abundance ratio of $[\text{HCO}^+/\text{H}_2] = 2.3 \times 10^{-9}$, while in the right of Fig. 4 it was obtained with HCO^+ abundance calculated with the method described before. Least squares fitting was employed for both plots, both of which presented tight correlations between the outflow mass traced by HCN 3-2 and HCO^+ 3-2.

4. DISCUSSION

4.1. Relationship between outflows and cores

A positive correlation between the outflow mass and the core mass was found in our sample with 23 sources, which was shown in the left pane Fig. 5. The mass of outflows (M_{out}) were traced by HCN 3-2, while the core mass were traced by H^{13}CN 3-2. The solid line is the result of least squares fitting, which is $M_{out} \sim 0.18 \times M_{core}^{0.77}$ with the correlation coefficient (R) of 0.92. Due to the inability to resolve distances along the line of sight, t_{dyn} of eight sources cannot be calculated. The right panel in Fig. 5 is the plot of the mass-loss rate \dot{M}_{out} traced by HCN 3-2 versus the core mass M_{core} traced by H^{13}CN 3-2 for 15 sources. The result of least squares fitting for mass-lose rate and core mass is $\dot{M}_{out} \sim 0.16 \times M_{core}^{0.75}$, with correlation coefficient (R) of 0.88.

The trend of increment of outflow mass with increasing core mass had been found with other tracers. ? used CO 2-1 to trace the outflow toward 26 massive star forming regions and found the correlation between the outflow mass and the core mass derived from the 1.2 mm dust emission. The best fit, spanning over three orders of magnitude in core mass, was $M_{out} \sim 0.1 \times M_{core}^{0.8}$. Maud et al. (2015b) mapped the outflows and cores of 65 Massive Young Stellar Objects (MYSOs), and compact H_{II} regions, resulting for core mass and outflow mass as $M_{out} \propto M_{core}^{0.8}$. C^{18}O 3-2 was used to establish the core mass and CO 3-2 was used to calculate the outflow mass in Maud et al. (2015a). Comparing the indices of the three power functions, it can be found that there is a similar trend between the outflows and cores in dense gas and those in large-scale gas.

The relationship between the mass of outflows and the core mass is sublinear with the index of ~ 0.8 , based on our results for dense outflowing molecular gas, as well as for total outflowing gas traced by CO lines (?Maud et al. 2015b). Such results indicate that dense gas fraction in such outflows may be similar and the ratio of outflowing gas and the gas in the cores decreases with increasing core mass. Further theoretical studies and large sample high-resolution observations are needed for understanding such sublinear relation.

4.2. Different outflow properties traced by different molecules

Outflowing molecular gas traced by different tracers, can reveal multiple phase of molecular outflows in massive star forming regions. Normally, molecular outflows traced by low- J CO are more extended than that traced by dense gas tracers, such as seen in G121.29+00.65 (L1287) with the SMA (Juárez et al. 2019) and in a sample of outflows with ALMA (Baug et al. 2021). In L1287 as an example, the blue wings of HCO^+ 1-0, CO 1-0 (Yang et al. 1991) and HCN 3-2 (see Fig. 4) exhibit higher intensity and larger spatial distribution compared to their corresponding red wings, while the HCO^+ 3-2 emission shows reversed wing characteristics. Additionally, similar spatial distribution of the blue and red wings of HCO^+ 1-0 and CO 1-0 emissions was reported in Yang et al. (1991), while the wings of HCO^+ 3-2 and HCN 3-2 present different separations to that of HCO^+ 1-0 and CO 1-0, with red lobe located in the northeast and blue lobe in the southwest (see Fig. 2). These differences may arise from variations in volume density and kinetic temperature of different outflowing gas. Line wings of dense gas tracers HCN 3-2 and HCO^+ 3-2 in this sample of massive star forming regions provide good candidates for further high-resolution observations to understand outflow properties and the feedback of massive formation in the future.

5. SUMMARY

With OTF mapping observations toward a sample of 33 massive star forming regions using 10-m SMT for HCN 3-2, HCO^+ 3-2, H^{13}CN 3-2, H^{13}CO^+ 3-2, we detected dense outflowing gas in 25 sources, with bipolar lobes in 18 sources and a single lobe in 3 sources seen with both HCN 3-2 and HCO^+ 3-2, while bipolar outflows only seen with HCO^+ 3-2 in two sources and only seen with HCN 3-2 in another sources. The outflow mass ranges from 0.28 to $165.4 M_{\odot}$, while

the core mass spans from 3.95 to 8730 M_{\odot} and the typical mass-loss rate is a few times $10^{-4} M_{\odot}\text{yr}^{-1}$. A sublinear tight correlation, with index of ~ 0.8 and correlation coefficient of 0.88, between the mass of dense molecular outflow and core mass, is found. The results of detected dense gas outflows provide a good sample for further high-resolution observations for studying outflows and star formation feedback during massive star forming process.

ACKNOWLEDGEMENTS

We would like to acknowledge the help of the staff of the 10-m SMT for assistance with the observations. This work is supported by National Key R&D Program of China under grant 2023YFA1608204 and the National Natural Science Foundation of China grant 12173067.

REFERENCES

- Arce, H. G. & Sargent, A. I. 2006, *ApJ*, 646, 1070.
doi:10.1086/505104
- Bally, J. 2016, *ARA&A*, 54, 491.
doi:10.1146/annurev-astro-081915-023341
- Baug, T., Wang, K., Liu, T., et al. 2021, *MNRAS*, 507, 4316. doi:10.1093/mnras/stab1902
- Beuther, H., Schilke, P., Sridharan, T. K., et al. 2002, *A&A*, 383, 892. doi:10.1051/0004-6361:20011808
- Blake, G. A., Sutton, E. C., Masson, C. R., et al. 1987, *ApJ*, 315, 621. doi:10.1086/165165
- Blake, G. A., Sandell, G., van Dishoeck, E. F., et al. 1995, *ApJ*, 441, 689. doi:10.1086/175392
- Bontemps, S. & Andre, P. 1997, *Herbig-Haro Flows and the Birth of Stars*, 182, 63
- Cabrit, S., Edwards, S., Strom, S. E., et al. 1990, *ApJ*, 354, 687. doi:10.1086/168725
- De Simone, M., Codella, C., Ceccarelli, C., et al. 2022, *MNRAS*, 512, 5214. doi:10.1093/mnras/stac083
- Gusdorf, A., Cabrit, S., Flower, D. R., et al. 2008, *A&A*, 482, 809. doi:10.1051/0004-6361:20078900
- Guerra-Varas, N., Merello, M., Bronfman, L., et al. 2023, *A&A*, 677, A148. doi:10.1051/0004-6361/202245522
- Heiderman, A., Evans, N. J., Allen, L. E., et al. 2010, *ApJ*, 723, 1019. doi:10.1088/0004-637X/723/2/1019
- Juárez, C., Liu, H. B., Girart, J. M., et al. 2019, *A&A*, 621, A140. doi:10.1051/0004-6361/201834173
- Konigl, A. & Pudritz, R. E. 2000, *Protostars and Planets IV*, 759. doi:10.48550/arXiv.astro-ph/9903168
- Kwan, J. & Scoville, N. 1976, *ApJL*, 210, L39.
doi:10.1086/182298
- Lada, C. J., Lombardi, M., & Alves, J. F. 2010, *ApJ*, 724, 687. doi:10.1088/0004-637X/724/1/687
- Li, Q., Zhou, J., Esimbek, J., et al. 2019, *MNRAS*, 488, 4638. doi:10.1093/mnras/stz2044 %bibitem[Li et al.(2022)]2022MNRAS.512.4934L Li, Y., Wang, J., Li, J., et al. 2022, *MNRAS*, 512, 4934.
doi:10.1093/mnras/stab3186
- Liu, H.-L., Sanhueza, P., Liu, T., et al. 2020, *ApJ*, 901, 31.
doi:10.3847/1538-4357/abadfe
- Liu, D.-J., Xu, Y., Li, Y.-J., et al. 2021, *ApJS*, 253, 15.
doi:10.3847/1538-4365/abcece
- Liu, S., Wang, J., Li, F., et al. 2023, *MNRAS*, 525, 4761.
doi:10.1093/mnras/stad2507
- Martin-Pintado, J., Bachiller, R., & Fuente, A. 1992, *A&A*, 254, 315
- Maud, L. T., Lumsden, S. L., Moore, T. J. T., et al. 2015, *MNRAS*, 452, 637. doi:10.1093/mnras/stv1334
- Maud, L. T., Moore, T. J. T., Lumsden, S. L., et al. 2015, *MNRAS*, 453, 645. doi:10.1093/mnras/stv1635
- Motte, F., Zavagno, A., Bontemps, S., et al. 2010, *A&A*, 518, L77. doi:10.1051/0004-6361/201014690
- Müller, H. S. P., Thorwirth, S., Roth, D. A., et al. 2001, *A&A*, 370, L49. doi:10.1051/0004-6361:20010367
- Müller, H. S. P., Schlöder, F., Stutzki, J., et al. 2005, *Journal of Molecular Structure*, 742, 215.
doi:10.1016/j.molstruc.2005.01.027
- Plume, R., Jaffe, D. T., Evans, N. J., et al. 1997, *ApJ*, 476, 730. doi:10.1086/303654
- Reid, M. J., Menten, K. M., Brunthaler, A., et al. 2014, *ApJ*, 783, 130. doi:10.1088/0004-637X/783/2/130
- Rodriguez, T. M., Hofner, P., Edelman, I., et al. 2021, 37th Annual New Mexico Symposium, 15
- Shepherd, D. S. & Churchwell, E. 1996, *ApJ*, 472, 225.
doi:10.1086/178057
- Shu, F. H., Adams, F. C., & Lizano, S. 1987, *ARA&A*, 25, 23. doi:10.1146/annurev.aa.25.090187.000323
- Shu, F. H., Najita, J. R., Shang, H., et al. 2000, *Protostars and Planets IV*, 789
- Skretas, I. M. & Kristensen, L. E. 2022, *A&A*, 660, A39.
doi:10.1051/0004-6361/202141944
- Skretas, I. M., Karska, A., Wyrowski, F., et al. 2023, *A&A*, 679, A66. doi:10.1051/0004-6361/202346825
- Wu, Y., Wei, Y., Zhao, M., et al. 2004, *A&A*, 426, 503.
doi:10.1051/0004-6361:20035767
- Yan, Y. T., Henkel, C., Kobayashi, C., et al. 2023, *A&A*, 670, A98. doi:10.1051/0004-6361/202244584
- Yang, J., Umemoto, T., Iwata, T., et al. 1991, *ApJ*, 373, 137. doi:10.1086/170032
- Zhang, Q., Hunter, T. R., Brand, J., et al. 2001, *ApJL*, 552, L167. doi:10.1086/320345
- Zhang, Q., Hunter, T. R., Brand, J., et al. 2005, *ApJ*, 625, 864. doi:10.1086/429660
- Zinchenko, I., Liu, S.-Y., Su, Y.-N., et al. 2015, *ApJ*, 810, 10. doi:10.1088/0004-637X/810/1/10
- Zuckerman, B., Kuiper, T. B. H., & Rodriguez Kuiper, E. N. 1976, *ApJL*, 209, L137. doi:10.1086/182284

Table 1. Basic information and data parameters of 33 sources

Source Alias	R.A.(J2000) (hh:mm:ss)	Decl.(J2000) (dd:mm:ss)	D (kpc)	D_{GC} (kpc)	Line (3-2)	$\int T_{\text{mb}} dv_{\text{Core}}^a$ ($\text{K} \cdot \text{km s}^{-1}$)	$\int T_{\text{mb}} dv_{\text{Blue}}^b$ ($\text{K} \cdot \text{km s}^{-1}$)	$\int T_{\text{mb}} dv_{\text{Red}}$ ($\text{K} \cdot \text{km s}^{-1}$)	v_{LSR} (km s^{-1})	Blue Range (km s^{-1})	Red Range (km s^{-1})
G121.29+00.65	00:36:47.35	63:29:02.2	0.93	8.8	HCN	5.28(0.33)	14.79(0.79)	6.71(0.56)	-18	-32 -22	-13 -8
					HCO ⁺	9.97(0.27)	8.39(0.81)	10.56(0.81)	-18	-30 -22	-13 -5
G123.06-06.30	00:52:24.70	56:33:50.5	2.82	10.1	HCN	2.98(0.16)	7.49(0.46)	4.06(0.4)	-31	-44 -35	-25 -18
					HCO ⁺	6.11(0.29)	5.00(0.41)	4.36(0.41)	-30	-43 -35	-25 -17
G183.72-03.60	05:40:24.23	23:50:54.7	1.75	10.1	HCN	0.48(0.12)	6.10(0.56)	7.25(0.6)	2	-7 0	4 12
					HCO ⁺	1.73(0.19)	6.99(0.37)	8.36(0.34)	2	-6 0	4 9
G005.88-00.39	18:00:30.31	-24:04:04.5	2.99	5.3	HCN	57.50(1.17)	49.91(1.25)	86.62(1.32)	11	-25 1	18 47
					HCO ⁺	49.90(0.60)	43.37(1.24)	91.94(1.49)	11	-24 1	18 54
G010.62-00.38	18:10:28.55	-19:55:48.6	4.95	3.6	HCN	53.41(0.54)	10.10(1.12)	19.03(1.17)	-3	-23 -13	6 17
					HCO ⁺	63.18(0.49)	5.03(0.81)	13.20(0.92)	-3	-20 -13	6 15
G011.91-00.61	18:13:58.12	-18:54:20.3	1.25	5.1	HCN	5.99(0.27)	12.87(1.08)	8.46(0.99)	37	16 29	44 55
					HCO ⁺	5.49(0.28)	3.21(0.91)	2.09(0.91)	36	22 29	44 51
G012.80-00.20	18:14:14.23	-17:55:40.5	2.92	5.5	HCN	74.06(0.96)	71.03(1.86)	102.29(2.38)	36	18 29	42 60
					HCO ⁺	108.30(0.69)	31.95(1.2)	49.62(1.47)	36	23 29	42 51
G015.03-00.67	18:20:24.81	-16:11:35.3	1.98	6.4	HCN	38.54(0.42)	31.65(0.75)	36.70(0.81)	20	7 13	26 33
					HCO ⁺	82.64(0.54)	31.02(1.29)	41.35(1.29)	20	5 13	26 34
G023.43-00.10	18:34:39.29	-08:31:25.4	5.88	3.7	HCN	8.40(0.47)	13.64(0.79)	14.60(0.97)	102	78 90	110 128
					HCO ⁺	10.16(0.52)	6.63(0.97)	5.59(0.91)	101	81 90	110 118
G023.00-00.41	18:34:40.20	-09:00:37.0	4.59	4.5	HCN	4.56(0.22)	11.39(0.67)	8.49(0.61)	76	57 70	85 96
					HCO ⁺	5.11(0.32)	13.87(0.75)	4.57(0.71)	75	59 70	85 95
G029.95-00.01	18:46:03.74	-02:39:22.3	5.26	4.6	HCN	13.29(0.26)	17.72(1.61)	10.94(1.53)	97	81 92	104 114
					HCO ⁺	9.76(0.24)	6.94(1.25)	4.70(1.25)	98	84 92	104 112
G032.04+00.00	18:49:36.58	-00:45:46.9	5.18	4.2	HCN	4.75(0.21)	14.39(1.23)	15.23(1.14)	95	73 88	102 115
					HCO ⁺	5.05(0.24)	4.54(0.68)	5.84(0.64)	94	79 88	102 110
G043.16+00.01	19:10:13.41	09:06:12.8	11.11	7.6	HCN	31.97(0.55)	7.96(1.17)	17.73(1.21)	8	-25 -11	25 40
					HCO ⁺	50.52(0.62)	15.95(0.91)	52.64(1.22)	8	-25 -11	25 50
G069.54-00.97	20:10:09.07	31:31:36.0	2.46	7.8	HCN	7.18(0.29)	11.04(0.91)	10.84(0.94)	12	-10 5	18 34
					HCO ⁺	17.76(0.43)	17.26(1.07)	16.93(1.04)	12	-11 5	18 33
G075.76+00.33	20:21:41.09	37:25:29.3	3.51	8.2	HCN	8.15(0.33)	14.53(0.73)	23.82(0.8)	-1	-19 -8	5 18
					HCO ⁺	8.50(0.36)	10.36(0.53)	17.41(0.59)	-1	-17 -8	5 16
G081.87+00.78	20:38:36.43	42:37:34.8	1.30	8.2	HCN	27.54(0.40)	18.51(1.2)	24.22(1.31)	10	-7 3	16 28
					HCO ⁺	38.70(0.38)	22.19(1.23)	25.91(1.23)	10	-6 3	16 25
G081.75+00.50	20:39:01.99	42:24:59.3	1.50	8.2	HCN	8.76(0.23)	26.05(0.42)	21.77(0.45)	-3	-15 -9	1 8
					HCO ⁺	18.94(0.33)	10.92(1.09)	16.32(1.18)	-4	-15 -9	1 8
G109.87+02.11	22:56:18.10	62:01:49.5	0.70	8.6	HCN	20.59(0.38)	16.27(0.91)	23.13(0.91)	-10	-28 -17	-4 7
					HCO ⁺	45.42(0.40)	58.56(2.48)	19.81(2.07)	-10	-40 -17	-4 20
G028.86+00.00	18:43:46.22	-03:35:29.6	7.41	4.0	HCN	3.57(0.06)	105
					HCO ⁺	4.25(0.08)	3.96(0.56)	5.26(0.52)	104	91 99	107 114
G043.79-00.12	19:11:53.99	09:35:50.3	6.02	5.7	HCN	3.49(0.04)	44
					HCO ⁺	4.21(0.04)	5.92(0.62)	5.09(0.52)	44	31 38	50 55
G031.28+00.00	18:48:12.39	-01:26:30.7	4.27	5.2	HCN	4.70(0.08)	6.54(1.01)	7.04(1.15)	109	92 102	115 128
G031.58+00.00	18:48:41.68	-01:09:59.0	4.90	4.9	HCN	2.74(0.06)	7.25(0.41)	10.86(0.67)	96	86 92	101 117
G188.94+00.88	06:08:53.53	21:38:28.7	2.10	10.4	HCN	4.85(0.11)	...	18.78(0.91)	3	...	7 15
					HCO ⁺	9.66(0.09)	...	20.37(0.65)	3	...	7 17
G009.62+00.19	18:06:14.66	-20:31:31.7	5.15	3.3	HCN	18.77(0.17)	...	20.22(0.81)	6	...	14 26
					HCO ⁺	14.01(0.11)	...	9.93(0.99)	6	...	14 30
G011.49-03.60	18:16:22.13	-19:41:27.2	1.25	7.1	HCN	2.44(0.05)	...	8.54(0.64)	11	...	13 23
					HCO ⁺	7.23(0.08)	...	5.83(0.44)	11	...	13 20

Notes. Columns are: the source names/coordinates, right ascension (R.A.), declination (Decl.), trigonometric parallax distance (D) (Reid et al. 2014), Galactocentric distance (D_{GC}), line, flux integral intensity of cores ($\int T_{\text{mb}} dv_{\text{Core}}$), flux integral intensity of blue wing ($\int T_{\text{mb}} dv_{\text{Blue}}$), flux integral intensity of red wing ($\int T_{\text{mb}} dv_{\text{Red}}$), velocity range of blue wing, velocity range of red wing. *a.* Calculations are conducted using H^{13}CO^+ or H^{13}CN 3-2. *b.* Calculations are conducted using HCO^+ or HCN 3-2.

Table 2: Observational parameters for each source of HCN 3-2, HCO⁺ 3-2

Source name	HCN 3-2				HCO ⁺ 3-2			
	$1 \sigma_{blue}$ K km s ⁻¹	$1 \sigma_{red}$ K km s ⁻¹	starting K km s ⁻¹	step K km s ⁻¹	$1 \sigma_{blue}$ K km s ⁻¹	$1 \sigma_{red}$ K km s ⁻¹	starting K km s ⁻¹	step K km s ⁻¹
G121.29+00.65	0.22	0.16	0.95	0.36	0.17	0.17	1.00	0.18
G123.06-06.30	0.14	0.12	0.70	0.26	0.14	0.14	0.50	0.20
G183.72-03.60	0.13	0.14	0.60	0.35	0.12	0.11	0.65	0.25
G005.88-00.39	0.40	0.43	2.00	6.00	0.35	0.42	2.00	6.00
G010.62-00.38	0.38	0.40	1.65	1.00	0.29	0.33	1.50	0.80
G011.91-00.61	0.35	0.32	1.30	0.45	0.24	0.24	0.80	0.25
G012.80-00.20	0.24	0.31	2.40	1.80	0.17	0.21	1.00	1.20
G015.03-00.67	0.14	0.15	1.10	0.50	0.16	0.16	1.10	0.60
G023.43-00.10	0.26	0.32	1.00	1.00	0.21	0.19	0.90	0.30
G023.00-00.41	0.21	0.19	1.15	0.40	0.21	0.20	0.75	0.50
G029.95-00.01	0.32	0.31	1.00	0.66	0.25	0.25	0.90	0.30
G032.04+00.00	0.27	0.25	1.20	0.80	0.21	0.20	0.75	0.35
G043.16+00.01	0.20	0.21	1.00	0.80	0.21	0.28	0.90	3.20
G069.54-00.97	0.27	0.28	0.90	0.80	0.24	0.23	0.75	1.10
G075.76+00.33	0.24	0.26	1.50	0.60	0.18	0.20	1.00	0.70
G081.87+00.78	0.26	0.28	1.50	0.80	0.22	0.22	1.20	1.00
G081.75+00.50	0.07	0.08	0.50	0.80	0.17	0.18	0.80	0.60
G109.87+02.11	0.27	0.27	2.48	0.50	0.38	0.32	3.00	2.00
G028.86+00.00	0.19	0.18	0.70	0.20
G043.79-00.12	0.17	0.15	0.47	0.15
G031.28+00.00	0.23	0.26	0.85	0.27
G031.58+00.00	0.14	0.23	0.93	0.30
G188.94+00.88	...	0.25	0.90	0.30	...	0.27	1.00	0.30
G009.62+00.19	...	0.31	1.00	1.10	...	0.32	0.96	1.00
G011.49-03.60	...	0.24	1.00	0.40	...	0.18	0.90	0.25

Table 3. Source characteristics of 33 sources

Source Alias	M_{Core} (M_{\odot})	Line	$f(X)$ (10^{-9})	t_{dyn} (10^4 yr)	M_{Blue} (M_{\odot})	M_{Red} (M_{\odot})	\dot{M}_{Blue} (10^{-4}) ($M_{\odot} \text{ yr}^{-1}$)	\dot{M}_{Red} (10^{-4}) ($M_{\odot} \text{ yr}^{-1}$)
G121.29+00.65	11.12(0.69)	HCN	5.00	1.44	0.49(0.03)	0.22(0.02)	0.34(0.02)	0.15(0.01)
		HCO ⁺	5.52	1.14	0.14(0.01)	0.18(0.01)	0.13(0.01)	0.16(0.01)
G123.06-06.30	63.63(3.42)	HCN	5.00	1.49	2.28(0.14)	1.24(0.12)	1.53(0.09)	0.83(0.08)
		HCO ⁺	5.99	1.39	0.46(0.04)	0.40(0.04)	0.54(0.04)	0.47(0.04)
G183.72-03.60	3.95(0.99)	HCN	5.00	1.92	0.72(0.07)	0.85(0.07)	0.37(0.03)	0.44(0.04)
		HCO ⁺	10.53	1.97	0.23(0.01)	0.28(0.01)	0.12(0.01)	0.14(0.01)
G005.88-00.39	918.75(18.69)	HCN	5.00	...	17.00(0.43)	29.60(0.45)
		HCO ⁺	2.53	...	16.90(0.48)	35.90(0.58)
G010.62-00.38	1929.15(19.5)	HCN	5.00	...	9.46(1.05)	17.80(1.10)
		HCO ⁺	3.45	...	5.34(0.86)	14.00(0.98)
G011.91-00.61	16.42(0.74)	HCN	5.00	...	0.77(0.06)	0.51(0.06)
		HCO ⁺	2.68	0.77	0.17(0.05)	0.11(0.05)	0.27(0.08)	0.18(0.08)
G012.80-00.20	1157.96(15.01)	HCN	5.00	1.09	23.30(0.61)	33.50(0.78)	21.40(0.56)	30.90(0.72)
		HCO ⁺	4.26	1.77	9.83(0.37)	15.30(0.45)	4.04(0.15)	6.28(0.19)
G015.03-00.67	301.61(3.29)	HCN	5.00	...	4.75(0.11)	5.51(0.12)
		HCO ⁺	6.25	3.15	3.52(0.15)	4.69(0.15)	0.69(0.03)	0.92(0.03)
G023.43-00.10	434(24.28)	HCN	5.00	1.51	18.10(1.05)	19.30(1.28)	12.00(0.69)	12.80(0.85)
		HCO ⁺	3.53	...	9.01(1.32)	7.60(1.24)
G023.00-00.41	157.94(7.62)	HCN	5.00	2.1	9.19(0.54)	6.85(0.49)	4.38(0.26)	3.27(0.24)
		HCO ⁺	3.27	1.55	6.60(0.36)	2.17(0.34)	6.45(0.35)	2.13(0.33)
G029.95-00.01	610.39(11.94)	HCN	5.00	...	18.80(1.70)	11.60(1.62)
		HCO ⁺	2.15	...	8.85(1.59)	6.00(1.59)
G032.04+00.00	202.3(8.94)	HCN	5.00	...	14.80(1.26)	15.60(1.17)
		HCO ⁺	3.11	...	2.68(0.40)	3.45(0.38)
G043.16+00.01	8730.22(150.19)	HCN	5.00	...	37.50(5.51)	83.60(5.70)
		HCO ⁺	4.61	...	38.40(2.19)	127.00(2.94)
G069.54-00.97	98(3.96)	HCN	5.00	0.79	2.56(0.21)	2.51(0.22)	3.22(0.27)	3.16(0.27)
		HCO ⁺	7.25	...	1.08(0.07)	1.06(0.07)
G075.76+00.33	233.73(9.46)	HCN	5.00	3.03	6.85(0.34)	11.20(0.38)	2.26(0.11)	3.71(0.13)
		HCO ⁺	3.04	3.06	4.40(0.23)	7.40(0.25)	1.53(0.08)	2.57(0.09)
G081.87+00.78	108.3(1.57)	HCN	5.00	0.48	1.20(0.08)	1.57(0.08)	2.47(0.16)	3.23(0.18)
		HCO ⁺	4.12	0.48	1.17(0.06)	1.36(0.06)	2.10(0.12)	2.45(0.12)
G081.75+00.50	45.88(1.2)	HCN	5.00	2.65	2.24(0.04)	1.87(0.04)	0.85(0.01)	0.71(0.01)
		HCO ⁺	6.33	...	0.39(0.04)	0.59(0.04)
G109.87+02.11	24.26(0.45)	HCN	5.00	0.38	0.31(0.02)	0.43(0.02)	0.81(0.05)	1.15(0.05)
		HCO ⁺	6.45	0.22	0.49(0.02)	0.17(0.02)	2.26(0.10)	0.77(0.08)
G028.86+00.00	303.91(5.11)	HCN	5.00
		HCO ⁺	3.81	4.07	6.33(0.90)	8.49(0.84)	1.55(0.22)	2.08(0.21)
G043.79-00.12	236.15(2.71)	HCN	5.00
		HCO ⁺	3.60	...	6.67(0.70)	5.73(0.59)
G031.28+00.00	151.70(2.58)	HCN	5.00	6.63	4.56(0.70)	4.91(0.80)	0.69(0.11)	0.74(0.12)
G031.58+00.00	113.06(2.48)	HCN	5.00	1.57	6.67(0.38)	9.99(0.62)	4.25(0.24)	6.37(0.39)
G188.94+00.88	58.54(1.33)	HCN	5.00	0.55	...	2.20(0.11)	...	3.98(0.19)
		HCO ⁺	6.07	0.57	...	1.15(0.04)	...	2.01(0.06)
G009.62+00.19	707.39(6.41)	HCN	5.00	20.50(0.82)
		HCO ⁺	2.20	13.40(1.34)
G011.49-03.60	8.11(0.17)	HCN	5.00	0.46	...	0.51(0.04)	...	1.10(0.08)
		HCO ⁺	9.27	0.54	...	0.11(0.01)	...	0.21(0.02)

Notes. Columns are: the source names/coordinates, core mass calculated by H^{13}CN , line, absolute fractional abundance $f(X)$ of a species X relative to the most abundant interstellar molecule, H_2 , defined by $f(X) = N(X)/N(\text{H}_2)$, dynamical timescale of outflow (t_{dyn}), flux integral intensity of cores ($\int T_{mb} dv_{Core}$), flux integral intensity of blue wing ($\int T_{mb} dv_{Blue}$), flux integral intensity of red wing ($\int T_{mb} dv_{Red}$), velocity range of blue wing, velocity range of red wing.

Table 4. Outflow properties of 33 sources

Source Alias	Line	P_{Blue} ($M_{\odot} \text{km s}^{-1}$)	P_{Red} ($M_{\odot} \text{km s}^{-1}$)	E_k_{Blue} ($M_{\odot} \text{km}^2 \text{s}^{-2}$)	E_k_{Red} ($M_{\odot} \text{km}^2 \text{s}^{-2}$)	F_{Blue} ($10^{-4} M_{\odot}$) ($\text{km s}^{-1} \text{yr}^{-1}$)	F_{Red} ($10^{-4} M_{\odot}$) ($\text{km s}^{-1} \text{yr}^{-1}$)
G121.29+00.65	HCN	4.48(0.24)	2.03(0.17)	20.57(1.10)	9.33(0.78)	3.11(0.17)	1.41(0.12)
	HCO+	1.34(0.13)	1.69(0.13)	6.13(0.59)	6.13(0.59)	1.17(0.11)	1.47(0.11)
G123.06-06.30	HCN	21.66(1.33)	11.74(1.16)	102.79(6.31)	102.79(5.49)	14.49(0.89)	7.86(0.77)
	HCO+	7.60(0.62)	6.63(0.62)	38.93(3.19)	38.93(3.19)	5.49(0.45)	4.79(0.45)
G183.72-03.60	HCN	3.28(0.30)	3.90(0.32)	7.52(0.69)	7.52(0.74)	1.71(0.16)	2.03(0.17)
	HCO+	1.02(0.05)	1.22(0.05)	2.27(0.12)	2.27(0.11)	0.52(0.03)	0.62(0.03)
G005.88-00.39	HCN	378.93(9.49)	657.63(10.02)	4212.03(105.49)	4212.03(111.40)
	HCO+	412.87(11.80)	875.24(14.18)	4992.24(142.73)	4992.24(171.51)
G010.62-00.38	HCN	149.77(16.61)	282.19(17.35)	1185.04(131.41)	1185.04(137.28)
	HCO+	61.37(9.88)	161.06(11.23)	472.16(76.03)	472.16(86.36)
G011.91-00.61	HCN	11.74(0.99)	7.72(0.90)	89.49(7.51)	89.49(6.88)
	HCO+	2.41(0.68)	1.57(0.68)	13.85(3.93)	13.85(3.93)	3.12(0.88)	2.03(0.88)
G012.80-00.20	HCN	314.73(8.24)	453.24(10.55)	2129.79(55.77)	2129.79(71.36)	290.02(7.59)	417.65(9.72)
	HCO+	84.00(3.15)	130.45(3.86)	491.80(18.47)	491.80(22.63)	47.35(1.78)	73.54(2.18)
G015.03-00.67	HCN	51.75(1.23)	60.01(1.32)	281.76(6.68)	281.76(7.21)
	HCO+	24.79(1.03)	33.04(1.03)	141.28(5.88)	141.28(5.88)	7.87(0.33)	10.49(0.33)
G023.43-00.10	HCN	354.15(20.51)	379.08(25.19)	3473.39(201.17)	3473.39(247.01)	234.88(13.60)	251.41(16.70)
	HCO+	128.02(18.73)	107.94(17.57)	1130.65(165.42)	1130.65(155.19)
G023.00-00.41	HCN	143.02(8.41)	106.61(7.66)	1112.47(65.44)	1112.47(59.58)	68.14(4.01)	50.79(3.65)
	HCO+	149.02(8.06)	49.10(7.63)	1110.65(60.06)	1110.65(56.85)	96.21(5.20)	31.70(4.93)
G029.95-00.01	HCN	234.20(21.28)	144.59(20.22)	1462.28(132.86)	1462.28(126.26)
	HCO+	122.90(22.14)	83.23(22.14)	756.04(136.17)	756.04(136.17)
G032.04+00.00	HCN	215.13(18.39)	227.69(17.04)	1565.33(133.80)	1565.33(124.01)
	HCO+	49.58(7.43)	63.78(6.99)	280.49(42.01)	280.49(39.54)
G043.16+00.01	HCN	1219.82(179.30)	2717.02(185.43)	19829.91(2914.70)	19829.91(3014.35)
	HCO+	1661.61(94.80)	5483.82(127.09)	28997.34(1654.39)	28997.34(2217.98)
G069.54-00.97	HCN	39.83(3.28)	39.11(3.39)	310.10(25.56)	310.10(26.40)	50.12(4.13)	49.21(4.27)
	HCO+	23.89(1.48)	23.44(1.44)	177.23(10.99)	177.23(10.68)
G075.76+00.33	HCN	89.30(4.49)	146.39(4.92)	582.18(29.25)	582.18(32.05)	29.49(1.48)	48.35(1.62)
	HCO+	60.40(3.09)	101.50(3.44)	389.08(19.90)	389.08(22.16)	19.71(1.01)	33.12(1.12)
G081.87+00.78	HCN	16.14(1.05)	21.12(1.14)	108.88(7.06)	108.88(7.71)	33.30(2.16)	43.58(2.36)
	HCO+	13.72(0.76)	16.02(0.76)	92.56(5.13)	92.56(5.13)	28.31(1.57)	33.06(1.57)
G081.75+00.50	HCN	20.20(0.33)	16.88(0.35)	90.99(F1.47)	90.99(1.57)	7.63(0.12)	6.37(0.13)
	HCO+	4.35(0.43)	6.50(0.47)	21.85(2.18)	21.85(2.36)
G109.87+02.11	HCN	4.03(0.23)	5.73(0.23)	26.64(1.49)	26.64(1.49)	14.21(2.03)	15.21(0.60)
	HCO+	11.26(0.48)	3.81(0.40)	127.59(5.40)	127.59(4.51)	51.25(2.17)	17.34(1.81)
G028.86+00.00	HCN
	HCO+	57.88(8.27)	77.67(7.68)	264.81(37.83)	355.33(35.13)	10.05(1.44)	19.07(1.88)
G043.79-00.12	HCN
	HCO+	68.28(7.15)	58.71(6.00)	349.57(36.61)	300.56(30.71)
G031.28+00.00	HCN	22.49(3.67)	15.90(2.60)	47.86(7.39)	51.52(8.42)	3.15(0.49)	3.39(0.55)
G031.58+00.00	HCN	222.14(13.70)	157.08(9.69)	1648.44(93.22)	2369.25(152.33)	141.68(8.74)	100.19(6.18)
G188.94+00.88	HCN	...	34.89(1.69)	...	276.10(13.38)	...	62.94(3.05)
	HCO+	...	17.72(0.57)	...	136.32(4.35)	...	30.97(0.99)
G009.62+00.19	HCN	...	313.21(12.55)	...	2387.45(95.64)
	HCO+	...	154.22(15.38)	...	887.65(88.50)
G011.49-03.60	HCN	...	6.92(0.52)	...	46.80(3.51)	...	14.89(1.12)
	HCO+	...	1.29(0.10)	...	7.54(0.57)	...	2.40(0.18)

Notes. Columns are: the source names/coordinates, line, the momentum of blue wing (P_{Blue}), the momentum of red wing (P_{Red}), the kinetic energy of blue wing (E_k_{Blue}), the kinetic energy of red wing (E_k_{Red}), the force of blue wing (F_{Blue}), the force of red wing (F_{Red}).

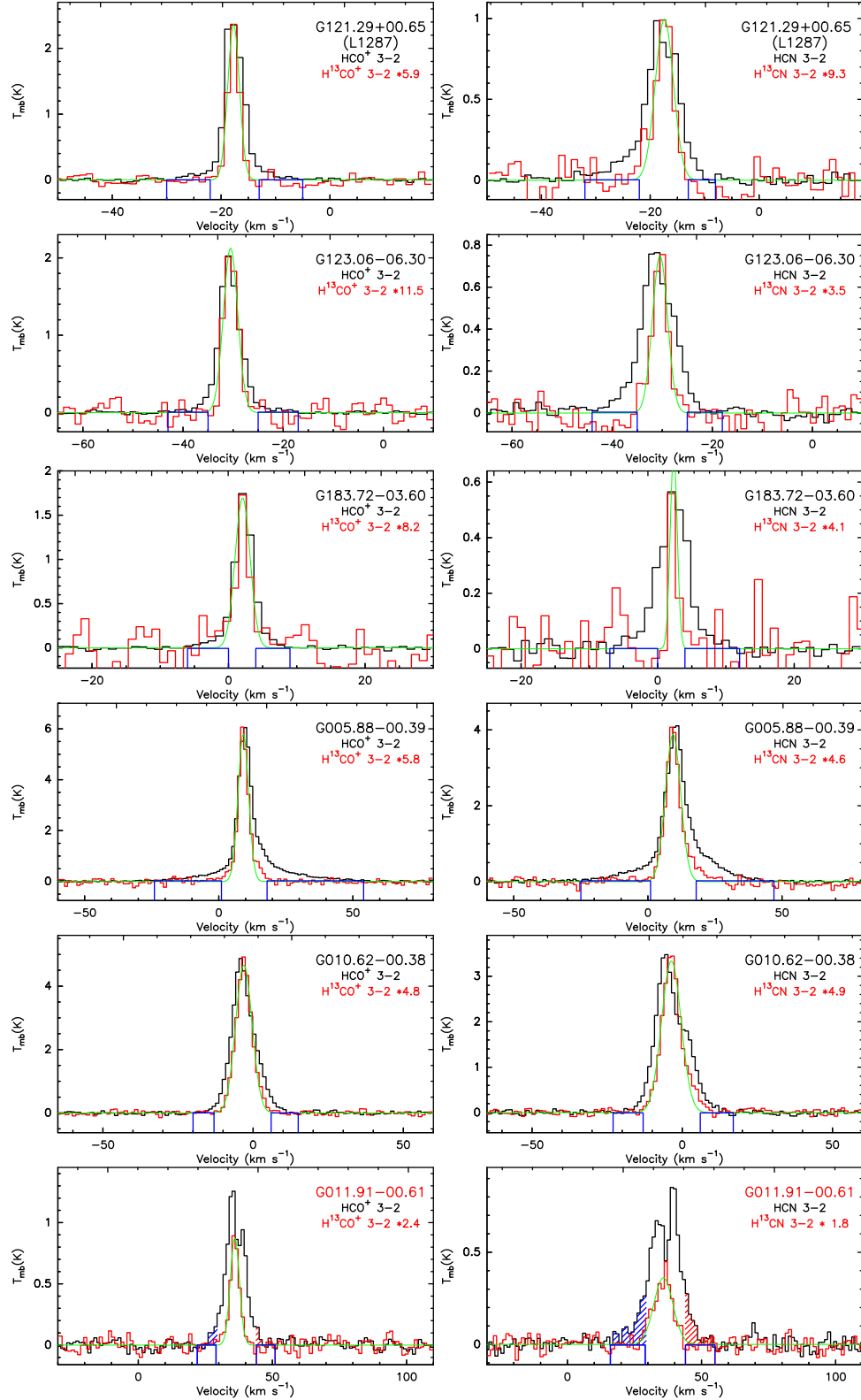


Figure 1: The averaged spectral lines of HCN and HCO⁺ 3-2. The source names are shown in the panels. Each panel presents the spectra of HCO⁺ or HCN (black) and H¹³CO⁺ or H¹³CN (red) 3-2 after averaging all the spectral lines within the signal area. The blue and red line wing emissions are labeled with blue windows. The green line is the Gaussian fitting of the spectral line of H¹³CO⁺ or H¹³CN 3-2.

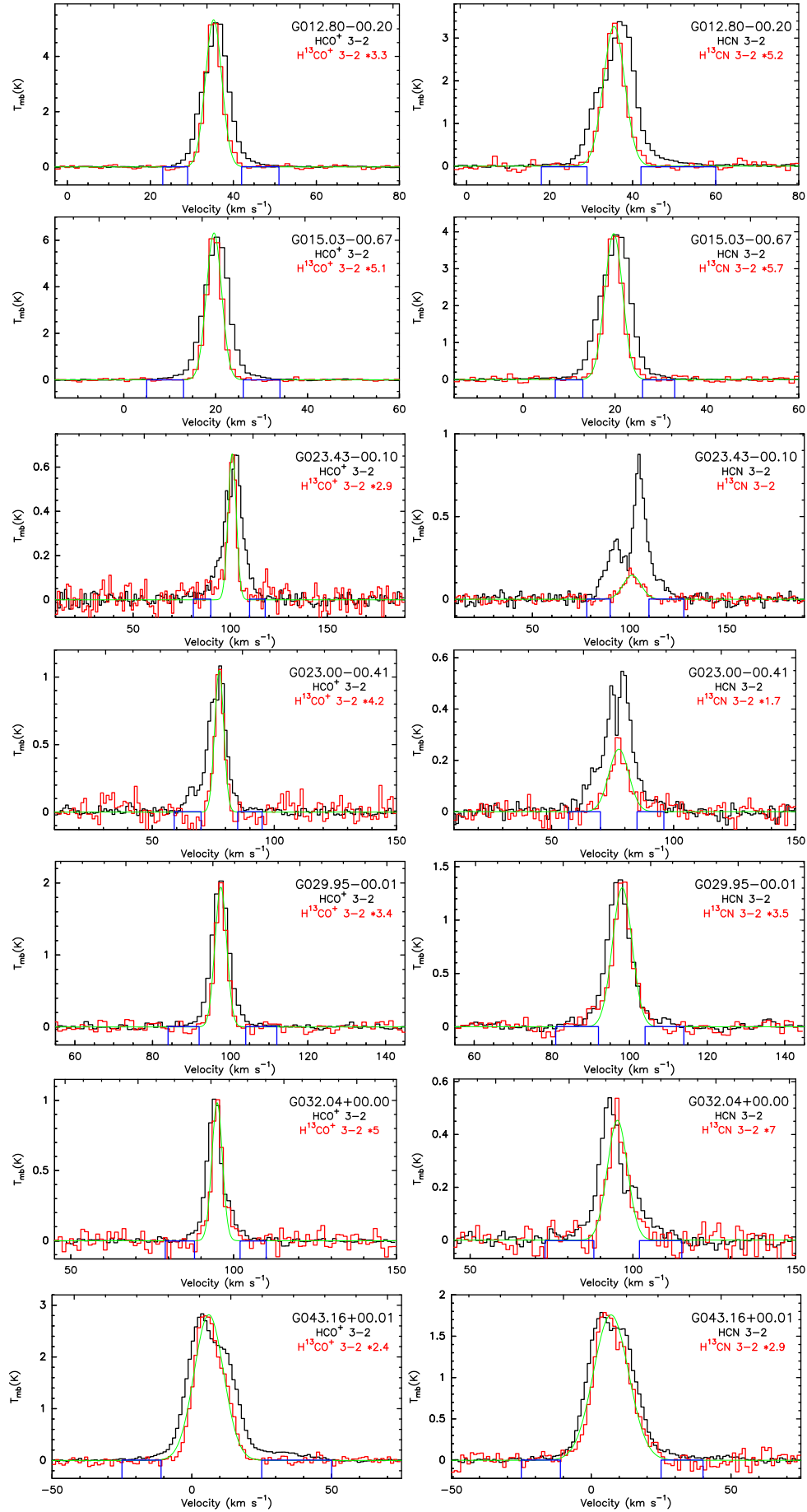


Figure 1: Continued.

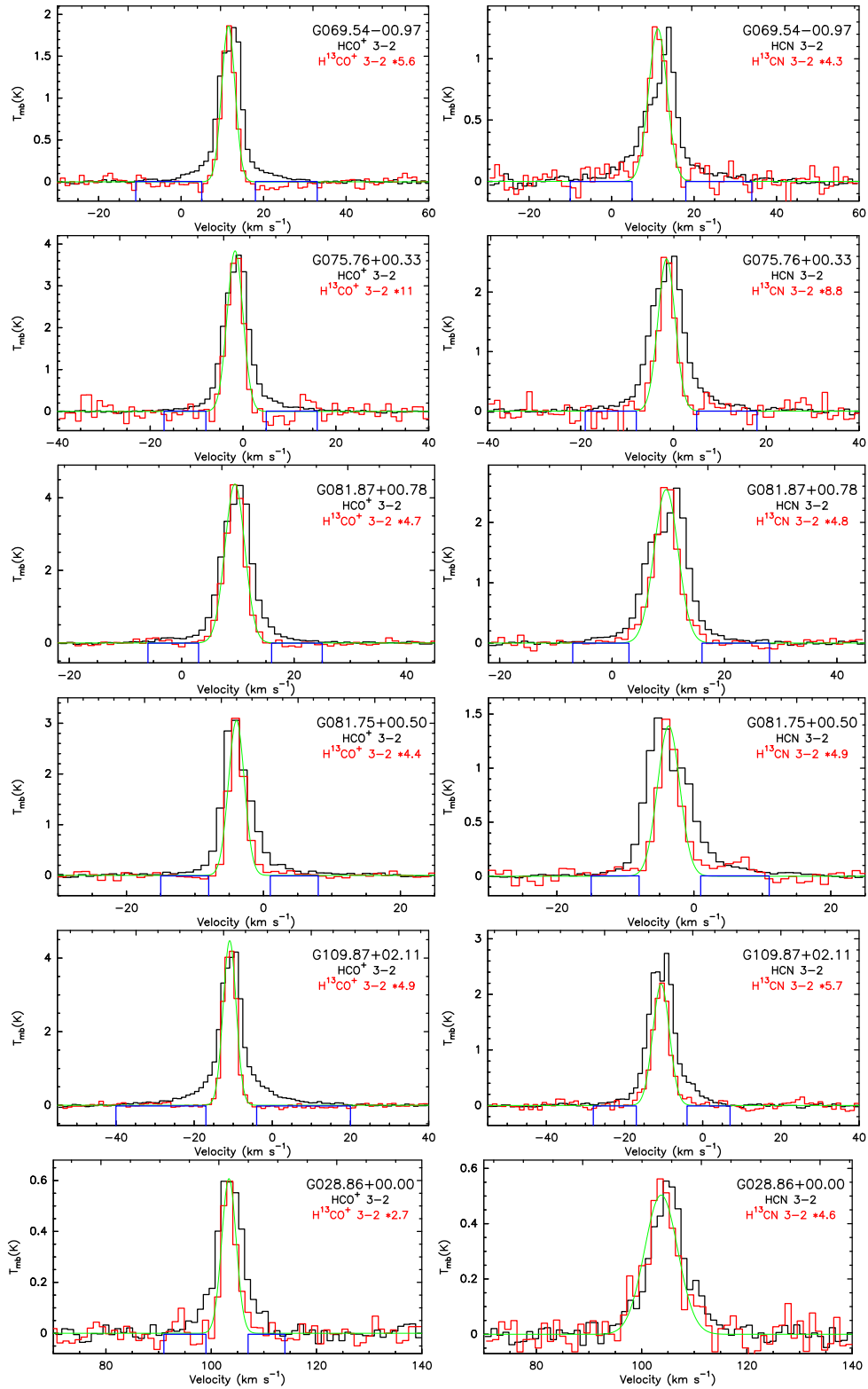


Figure 1: Continued.

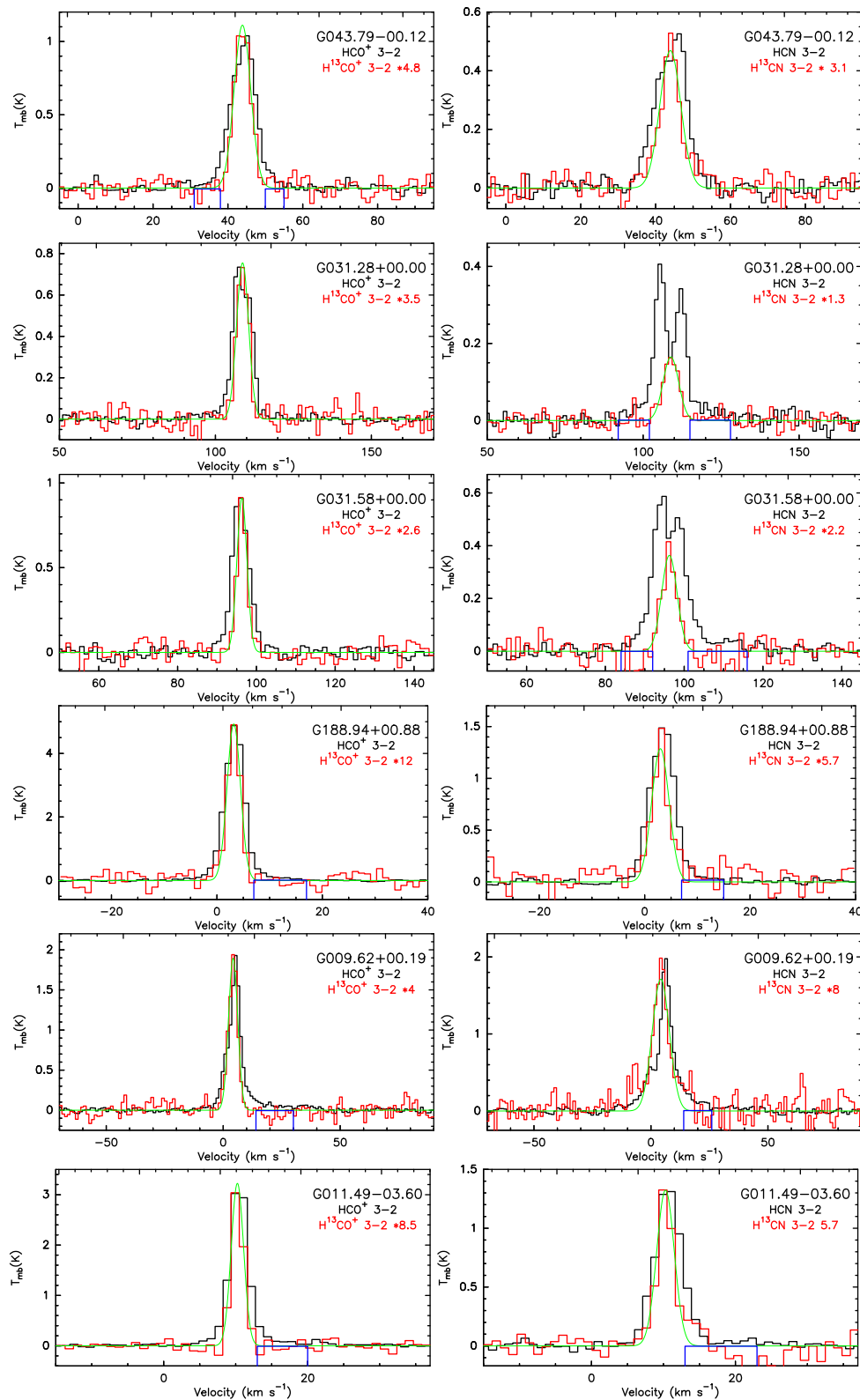


Figure 1: Continued.

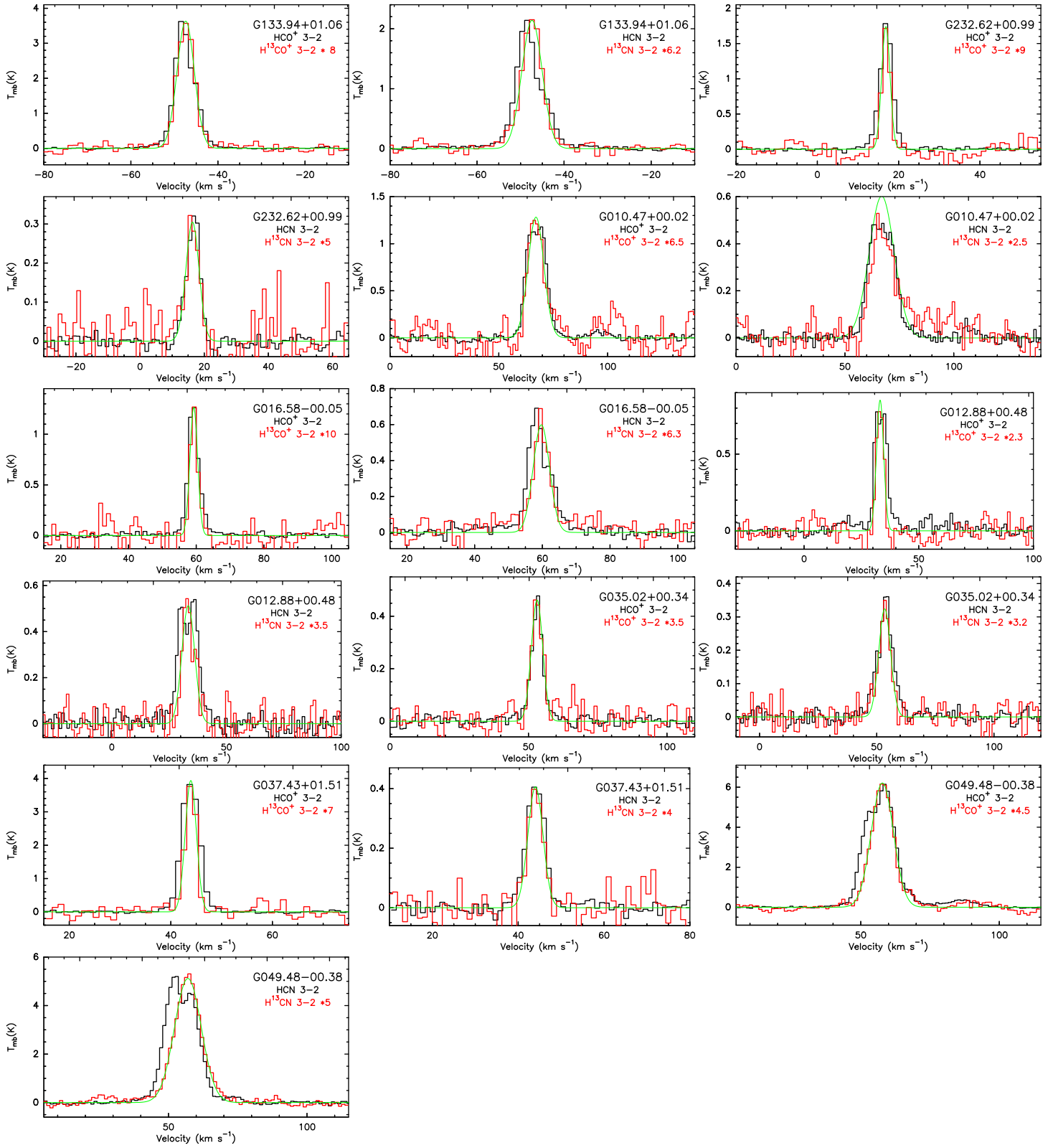


Figure 1: Continued.

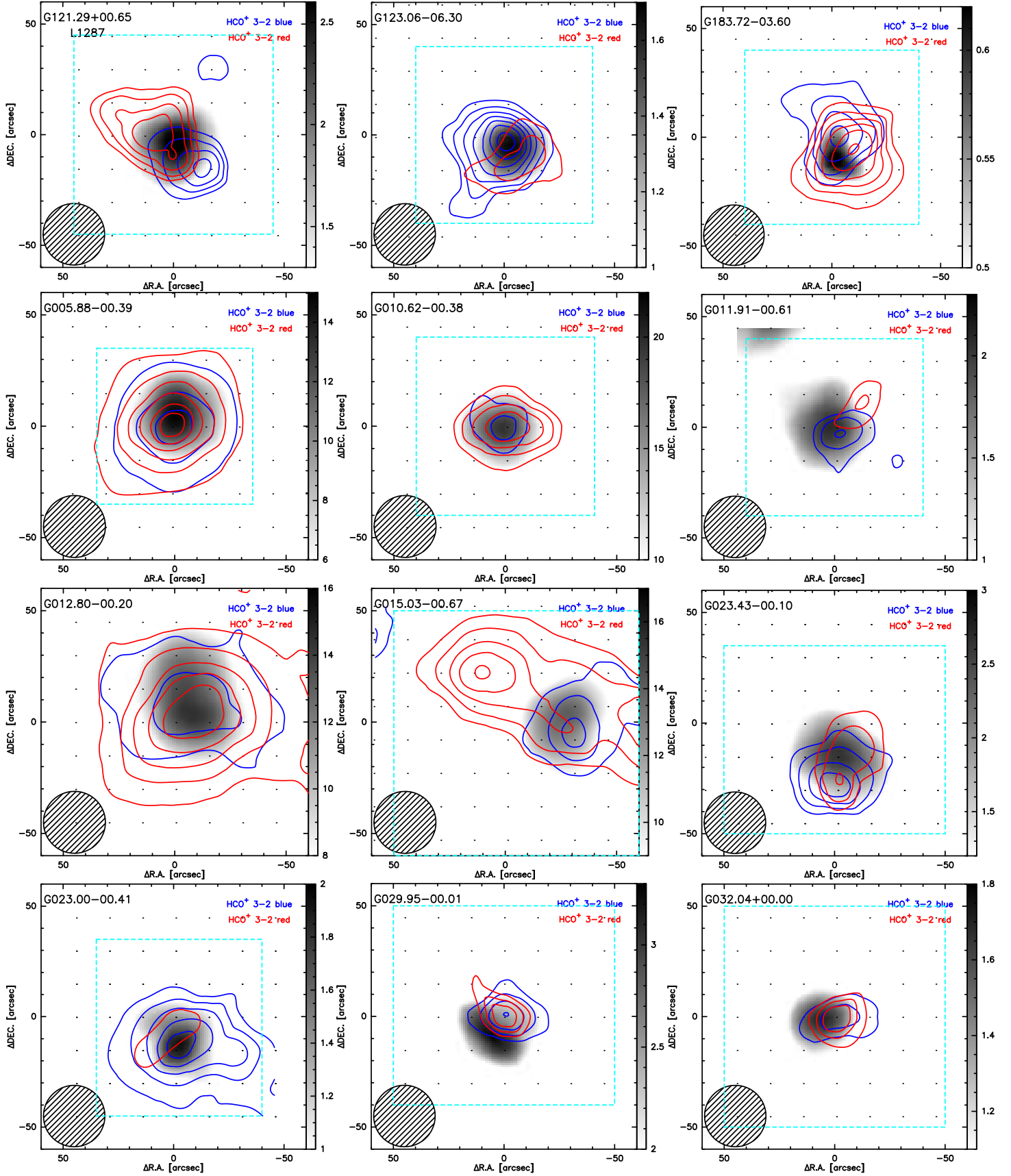


Figure 2: The line wing spatial distributions of HCO^+ 3-2. The source names are shown in the panels. Each panel shows the velocity integrated intensity distribution of blue and/or red wings traced by HCO^+ 3-2. The greyscales illustrate the positions of cloud cores traced by H^{13}CO^+ 3-2. The cyan dotted line boxes indicate signal coverage. The detailed parameters for maps of this and other sources are presented in Table 4.

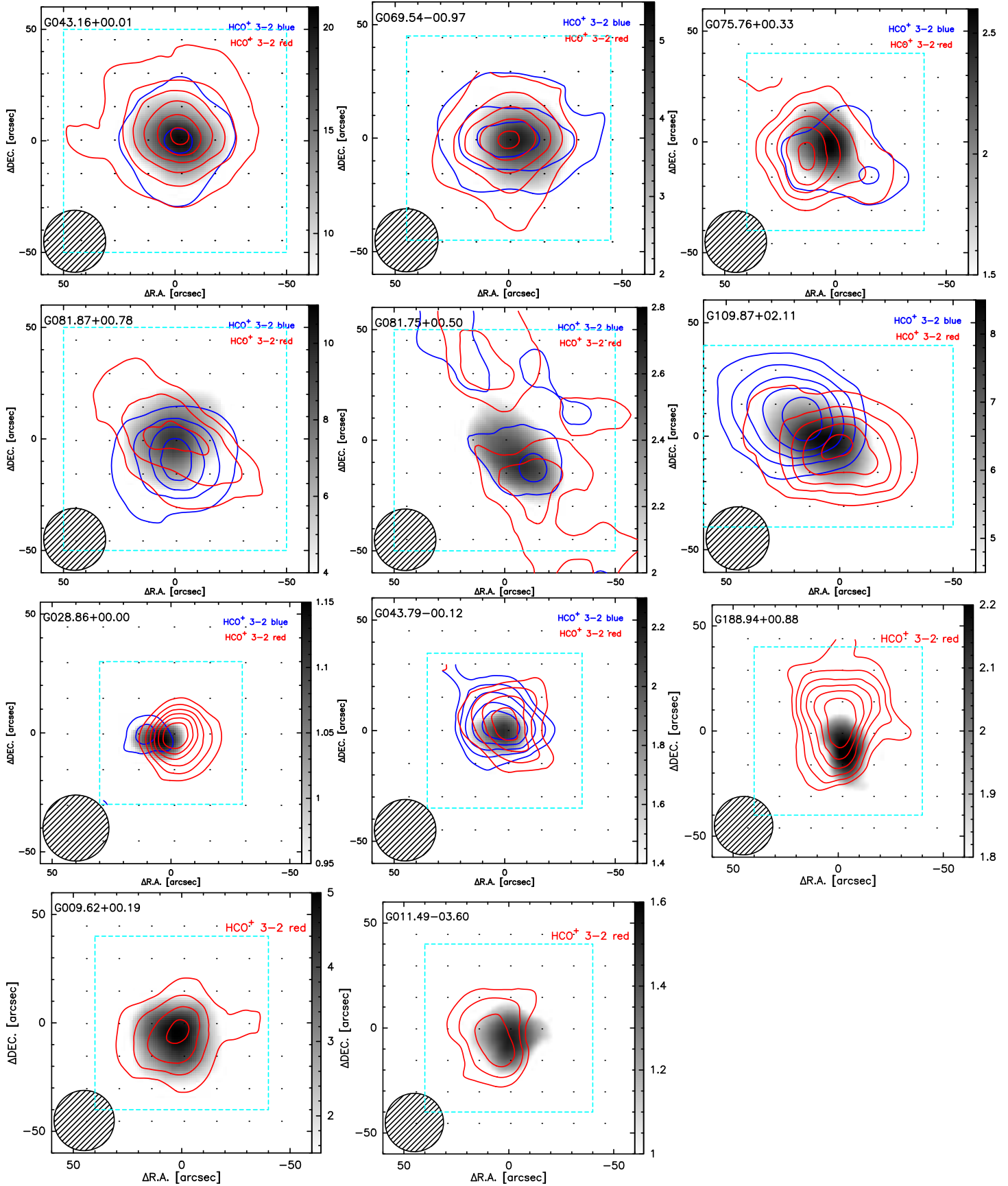


Figure 2: Continued.

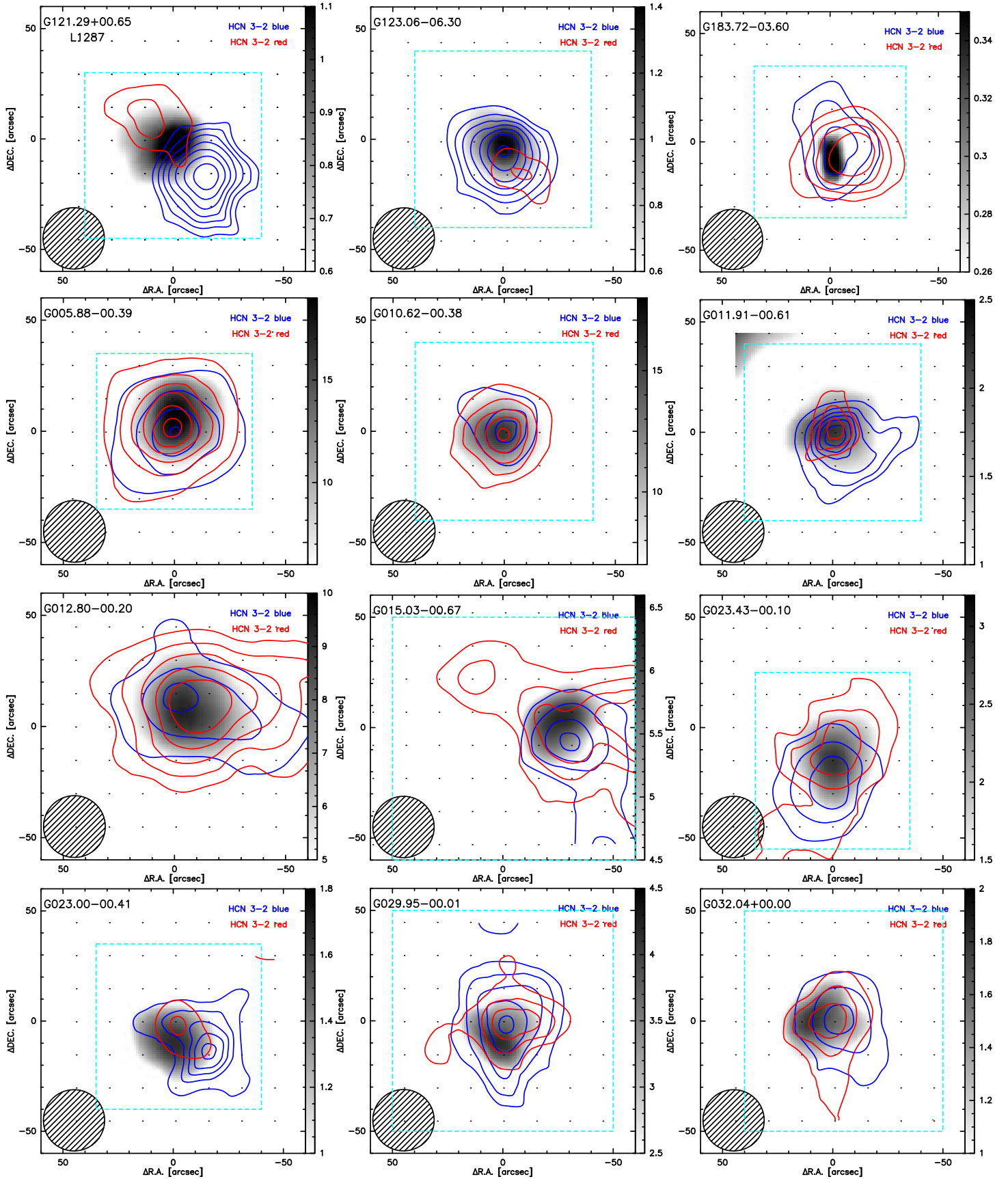


Figure 3: The line wing spatial distributions of HCN 3-2. The source names are shown in the panels. Each panel shows the velocity integrated intensity distribution of blue and/or red wings traced by HCN 3-2. The greyscales illustrate the positions of cloud cores traced by H¹³CN 3-2. The cyan dotted line boxes indicate signal coverage. The detailed parameters for maps of this and other sources are presented in Table 4.

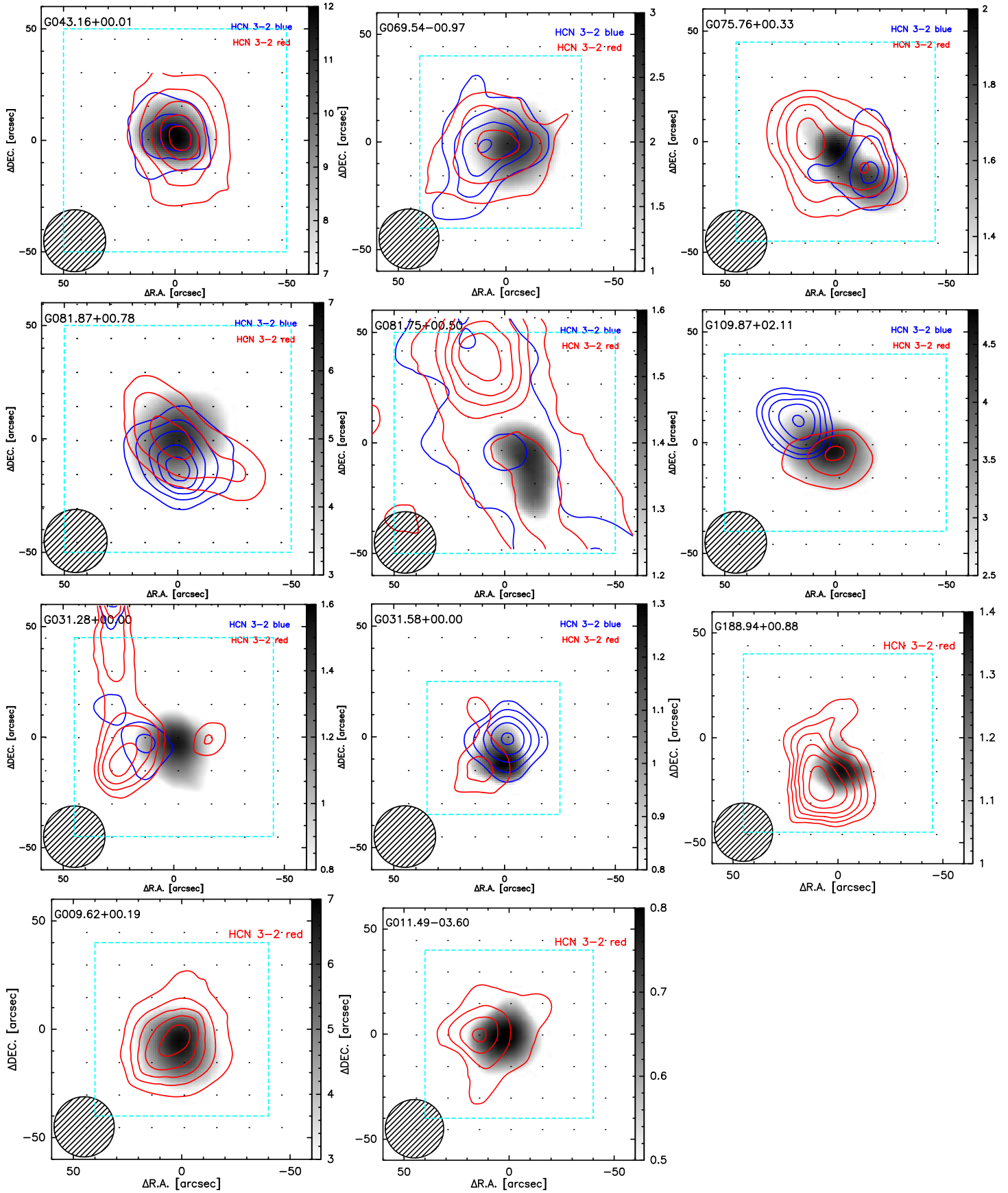


Figure 3: Continued.

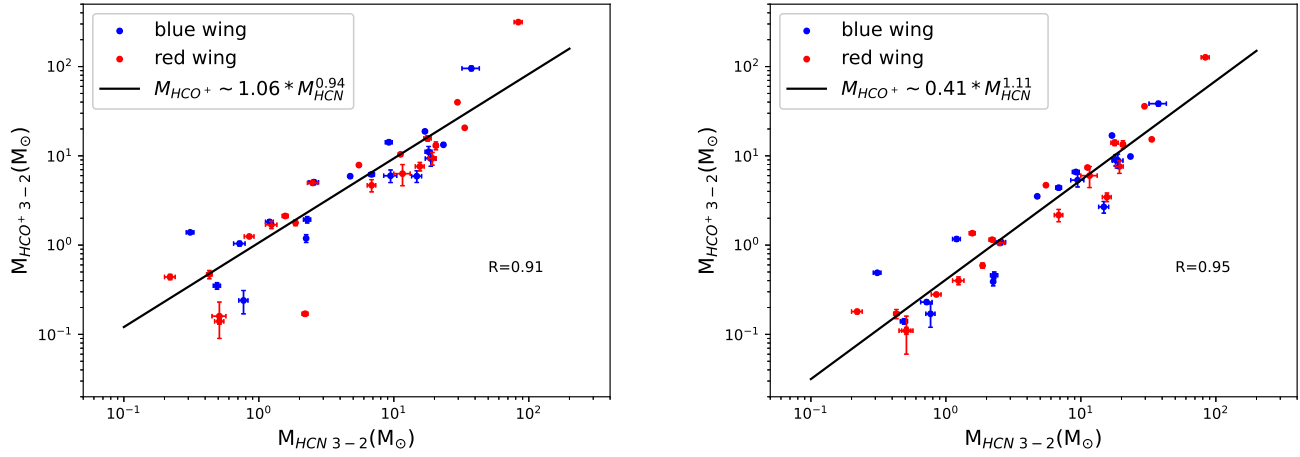


Figure 4: The relationship between the outflow mass traced by HCO^+ 3-2 and HCN 3-2 for 33 sources. In the left, outflow mass traced by HCO^+ 3-2 is obtained with fixed HCO^+ abundance, while it is unfixed to derive outflow mass traced by HCO^+ 3-2 in the right. The solid lines represent the fitting results.

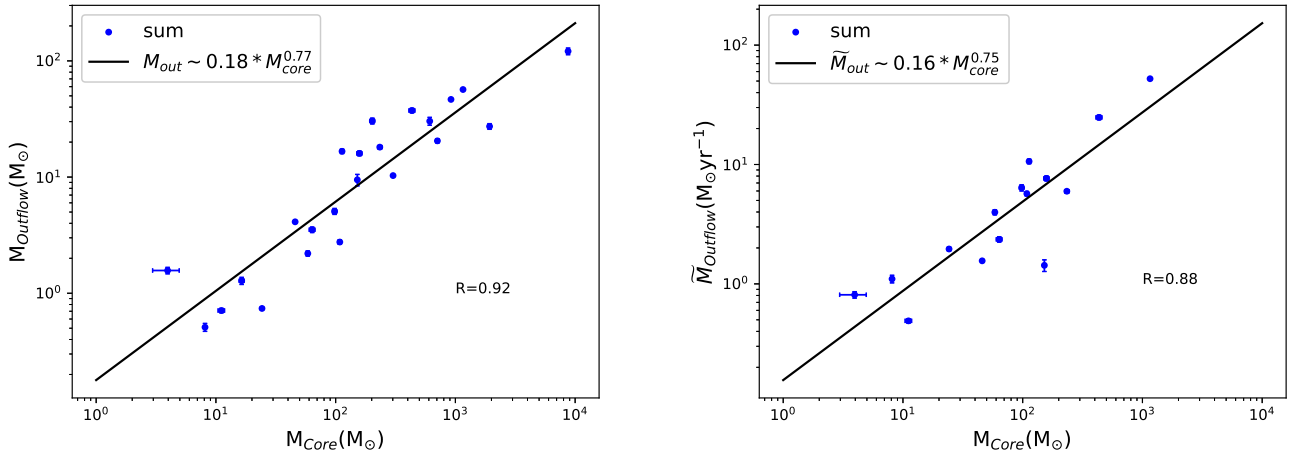


Figure 5: The left panel presents the outflow mass versus the cloud core mass for 23 sources. The right panel presents the mass loss rate versus the cloud core mass for 15 sources. The solid lines are obtained through linear regression using the least squares method.